Supplement Material

Kenta Kiuchi,[1,2] Sho Fujibayashi,[1] Kota Hayashi,[2] Koutarou Kyutoku,[3,4,5] Yuichiro Sekiguchi,[6,2] and Masaru Shibata[1,2]

[1] *Max Planck Institute for Gravitational Physics (Albert Einstein Institute), Am Mühlenberg, Potsdam-Golm, 14476, Germany*

[2] *Center for Gravitational Physics and Quantum Information, Yukawa Institute for Theoretical Physics, Kyoto University, Kyoto 606-8502, Japan*

[3] *Center for Gravitational Physics, Yukawa Institute for Theoretical Physics, Kyoto University, Kyoto 606-8502, Japan*

[4] *Department of Physics, Kyoto University, Kyoto 606-8502, Japan*

[5] *Interdisciplinary Theoretical and Mathematical Science Program (iTHEMS), RIKEN, Wako, Saitama 351-0198, Japan*

[6] *Department of Physics, Toho University, Funabashi, Chiba 274-8510, Japan*

(Dated: June 27, 2023)

DETAILED SETUP FOR SIMULATION

For the relativistic magnetohydrodynamic solver, the cell reconstruction method is the piece-wise parabolic method [1]. Because any high-resolution shock-capturing schemes based on the conservation law do not allow the vacuum state, we need to add a tenuous but low-density atmosphere during the simulations. We set the constant atmosphere with $\rho_{\rm atm} = 10^3$ g cm^{-3} for $r \le L_{13}$ and assume the power-law profile with $\rho_{\rm atm} = 10^3(L_{13}/r)^3$ g cm^{-3} for $r > L_{13} = 37.875$ km outside the NSs. Once $\rho_{\rm atm}$ reaches the floor value of the density of ≈ 0.166 g cm^{-3}, we assume the constant density profile. The atmosphere temperature is set to be 10^{-3} MeV.

In our fixed mesh refinment setup for the computational domains, the location of the outer boundary along each axis is $\approx 155,000$ km, and the *bulk* of the ejecta does not escape from the simulation domain during the simulation time of ≈ 1.1 s.

With the reflux prescription and divergence-free-prolongation, the baryonic mass is conserved with an error of $O(10^{-6}\%)$. The magnetic-flux conservation and the divergence-free condition are also satisfied with the machine precision.

EVOLUTION OF THE SYSTEM

Figure 1 is the same as Fig. 1 in the Letter, but for the different time slices with $t - t_{\rm merger} \approx 0.5$ s in the 1st and 2nd rows, and $t - t_{\rm merger} \approx 0.8$ s in the 3rd and 4th rows.

The left panel of Fig. 2 plots GWs for $l = m = 2$ mode with a hypothetical distance to the source of 100 Mpc.

The right panel of Fig. 2 plots the plasma beta profile defined by $\beta_{\rm plasma} \equiv P/b^\mu b_\mu$ at $t - t_{\rm merger} \approx 0.31$ s corresponding to the post-merger emergent time.

We do not find the launch of the Poynting-flux dominated outflow to the polar direction due to the Blandford-Znajek mechanism [2] throughout the simulation. It is in contrast to our recent BH-NS merger simulations [3], which show the launch of the Poynting-flux dominated outflow. The possible reasons for this qualitative difference are: (i) the BH spin is not very high compared to the BH-NS merger remnants; the dimensionless BH spin is $\approx 0.84 - 0.85$ in Ref. [3]. Moderately rapidly spinning BH found in this simulation can not wrap the magnetic field efficiently. However, note that the employed resolution is insufficient to suppress a spurious spin down of ≈ 0.15 as shown in the left panel of Fig. 3. (ii) for the BNS merger, the morphology of the dynamical ejecta is quasi-spherical. In particular, the shocked component is driven to the polar direction [4], which is absent for the BH-NS merger. A part of the shocked component falls back to the BH [5], and the ram pressure due to the fall-back material prevents earlier outflow by the magnetic pressure as shown in the right panel of Fig. 3 where we define the ratio of the ram pressure to the magnetic pressure by $\beta_{\rm ram} \equiv \rho (v^r)^2/b^\mu b_\mu$. We find that $\sigma_B \approx 1$ at most in the polar direction at the end of the simulation. However, the density of the polar region is still decreasing at the end of the simulation.

The left panel of Fig. 4 plots the cooling effciency defined by $L_\nu/(\dot{M}_{\rm acc} c^2)$ where $\dot{M}_{\rm acc}$ denotes the mass accretion rate on the BH. The cooling efficiency starts to decreases at $t - t_{\rm merger} \approx 0.1$–$0.2$ s [6–8]. The decrease becomes steep for $t - t_{\rm merger} \gtrsim 0.4$ s.

The right panel of Fig. 4 plots the evolution of the MADness parameter defined by [9]

$$\Phi_B \equiv \oint_{r=\max(r_{\rm AH})} \sqrt{\gamma} B^r r^2 \sin\theta d\theta d\phi. \qquad (0.1)$$

Although it is less than the critical value of the MAD state of $\Phi_B/(M_{\rm BH}^2 \dot{M}_{\rm acc})^{1/2} < 50$ [9], it still increases with time due to the suppression of the mass accretion rate. Therefore, the current simulation time may not be long enough to launch the Poynting-flux dominated outflow.

EJECTA CRITERIA

In this paper, we employ the Bernoulli criteria with $hu_t < -h_{\rm min}$ as ejecta criteria. $h_{\rm min}$ is the minimum

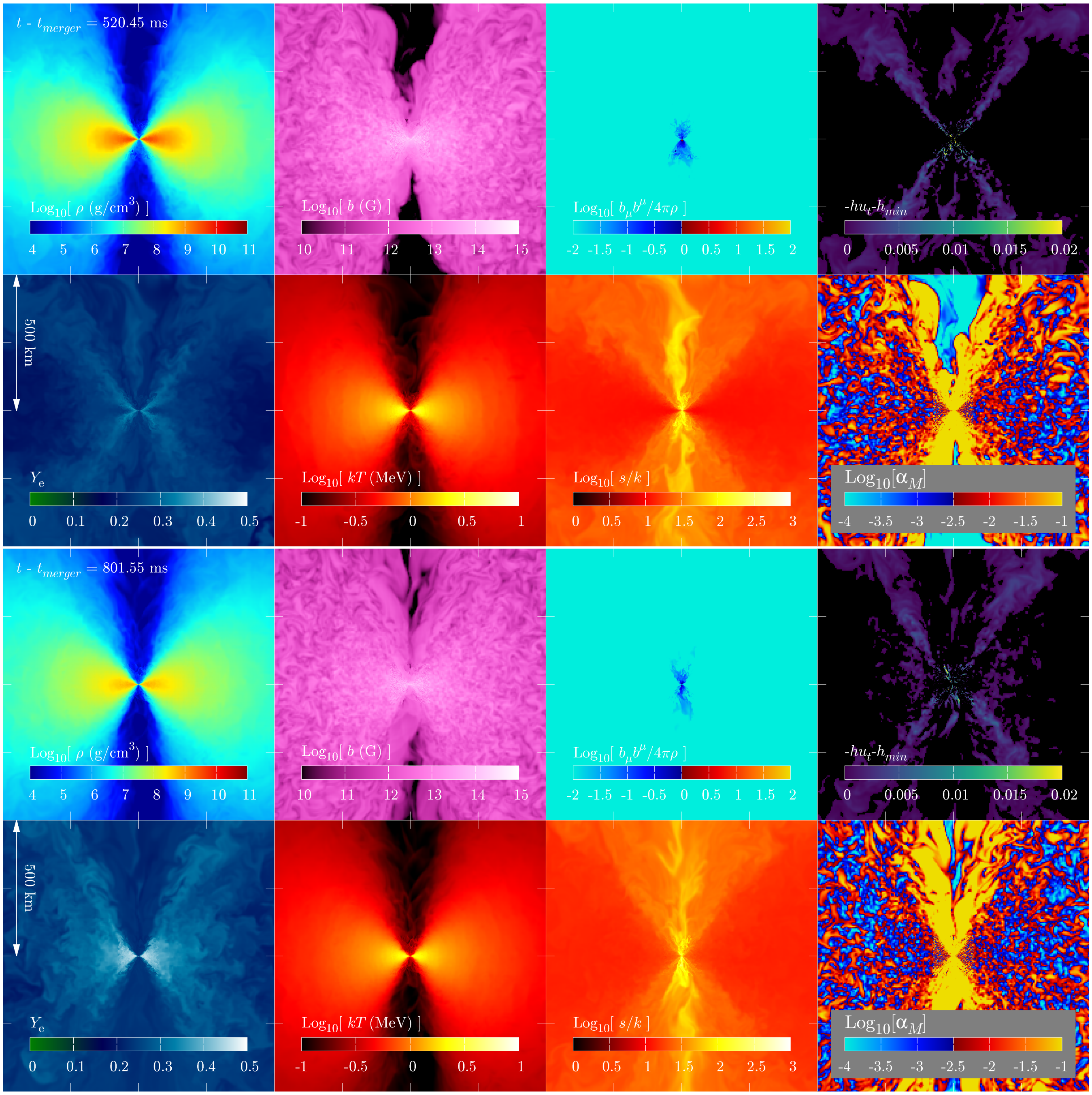

FIG. 1. Profiles for rest-mass density (top-left), magnetic-field strength (top-second from left), magnetization parameter (top-second from right), unboundness defined by the Bernoulli criterion (top-right), electron fraction (bottom-left), temperature (bottom-second from left), entropy per baryon (bottom-second from right), and Shakura-Sunyaev $\alpha_{\rm M}$ parameter (bottom-right) on the $y - y_{\rm AH} = 0$ plane at $t - t_{\rm merger} \approx 0.5$ s (the 1st- and 2nd-rows), and ≈ 0.8 s (the 3rd- and 4th-row).

value of the specific enthalpy given by an employed EOS. For the SFHo EOS, $h_{\rm min} = 0.9987$.

TRACER PARTICLE METHOD

A post-process tracer particle method is applied to generate the mass distributions of electron fraction $Y_{\rm e}$ and entropy per baryon s/k. In this method, 1316 tracer particles are placed on the sphere with the extraction radius $r_{\rm ext} = 10^9$ cm at every certain time interval $\Delta t_{\rm set}$ and

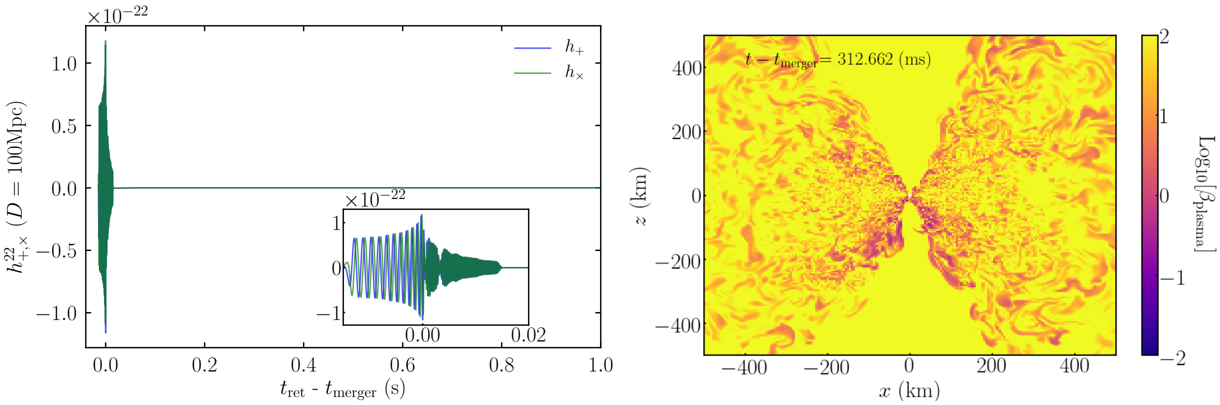

FIG. 2. (Left) $h_{+,\times}$ for $l = m = 2$ mode with a hypothetical distance to the source of 100 Mpc. The inset shows the waveforms around the merger time. (Right) Profile for the plasma beta at $t - t_{\rm merger} \approx 0.31$ s. The right panel shows the profile on the $y - y_{\rm AH} = 0$ plane where $y_{\rm AH}$ denotes the y coordinate of location of the puncture point.

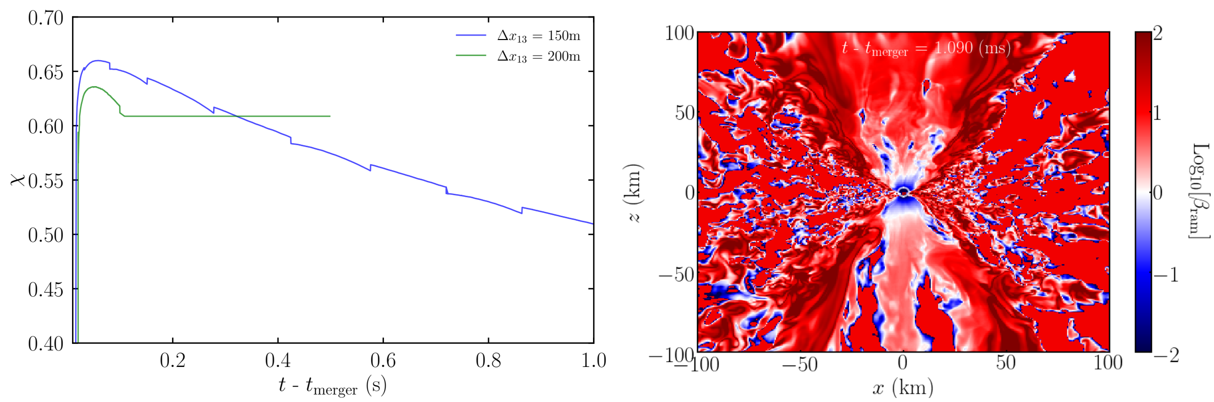

FIG. 3. (Left) Evolution of the dimensionless BH spin. Small discontinuous jumps are observed when the puncture point migrates by the grid size, Δx_{13}. The green curve denotes the low resolution run, in which the Cowling approximation is adopted for $t - t_{\rm merger} \gtrsim 0.1$ s. (Right) Profile for the ratio of the ram pressure to the magnetic pressure at $t - t_{\rm merger} \approx 1$ s on the $y - y_{\rm AH} = 0$ plane where $y_{\rm AH}$ denotes the y coordinate of location of the puncture point. The fluid elements with $v^r < 0$ are only shown.

evolved backward in time until the merger. The mass of each particle is defined as $\Delta m = \rho v^r {r_{\rm ext}}^2 \Delta\Omega \Delta t_{\rm set}$, where $\Delta\Omega \approx 0.01$ str is the solid angle element. To sample the particles efficiently, the time interval $\Delta t_{\rm set}$ is controlled as $\Delta t_{\rm set} \propto 1/\langle v^r \rangle$, where $\langle v^r \rangle$ is the average radial velocity of the ejecta at $r = r_{\rm ext}$.

The particles are evolved backward in time with an implicit method. For a given three-dimensional position $x^{i(n+1)}$ (i is the spatial index) of a particle at a time $t = t^{(n+1)}$, its position at $t = t^{(n)}$ ($< t^{(n+1)}$) is calculated by implicitly solving

$$\frac{x^{i(n+1)} - x^{i(n)}}{t^{(n+1)} - t^{(n)}} = \frac{1}{2}\left(v^{i(n)}(x^{(n)}) + v^{i(n+1)}(x^{(n+1)}) \right). \tag{0.2}$$

Here, $v^{i(n)}(x)$ is the coordinate velocity at the position x and the time $t = t^{(n)}$, which is interpolated trilinearly in spatial coordinates.

We define dynamical ejecta as the unbound matter that pass through the radius $r = 10^9$ cm until $t - t_{\rm merger} = 0.67$ s, which corresponds to the component that has the velocity higher than $0.05c$. The post-merger component is defined as all the other component.

[1] P. Colella and P. R. Woodward, Journal of Computational Physics **54**, 174 (1984).
[2] R. D. Blandford and R. L. Znajek, Mon. Not. Roy. Astron. Soc. **179**, 433 (1977).
[3] K. Hayashi, S. Fujibayashi, K. Kiuchi, K. Kyutoku, Y. Sekiguchi, and M. Shibata, (2021), arXiv:2111.04621 [astro-ph.HE].
[4] Y. Sekiguchi, K. Kiuchi, K. Kyutoku, and M. Shibata, Phys. Rev. D **91**, 064059 (2015), arXiv:1502.06660 [astro-ph.HE].

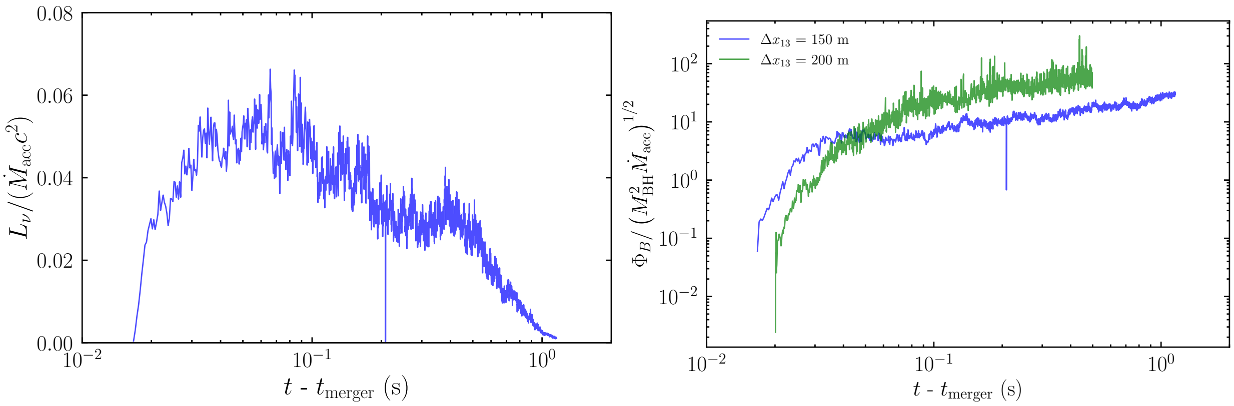

FIG. 4. Evolution of the cooling efficiency (left) and MADness parameter (right). The green curve in the right panel denotes the result in the low resolution run.

[5] W. Ishizaki, K. Kiuchi, K. Ioka, and S. Wanajo, Astrophys. J. **922**, 185 (2021), arXiv:2104.04708 [astro-ph.HE].

[6] O. Just, A. Bauswein, R. A. Pulpillo, S. Goriely, and H. T. Janka, Mon. Not. Roy. Astron. Soc. **448**, 541 (2015), arXiv:1406.2687 [astro-ph.SR].

[7] O. Just, S. Goriely, H.-T. Janka, S. Nagataki, and A. Bauswein, Mon. Not. Roy. Astron. Soc. **509**, 1377 (2021), arXiv:2102.08387 [astro-ph.HE].

[8] S. Fujibayashi, K. Kiuchi, S. Wanajo, K. Kyutoku, Y. Sekiguchi, and M. Shibata, (2022), arXiv:2205.05557 [astro-ph.HE].

[9] A. Tchekhovskoy, R. Narayan, and J. C. McKinney, Mon. Not. Roy. Astron. Soc. **418**, L79 (2011), arXiv:1108.0412 [astro-ph.HE].